FRACTURE RESISTANCE OF CAST AUSTENITIC STAINLESS STEELS

Y. Chen,[1] W-Y. Chen, [1] Z. Li, [2] Y. Yang, [2] B. Alexandreanu, [1] K. Natesan, [1] and A. S. Rao [3]

[1] Argonne National Laboratory, Lemont, IL 60439
[2] University of Florida, Gainesville, FL 32608
[3] Nuclear Regulatory Commission, Rockville, MD 20852

Abstract

Cast austenitic stainless steels (CASS) possess excellent corrosion resistance and mechanical properties and are used alongside with wrought stainless steels (SS) in light water reactors for primary pressure boundaries and reactor core internal components. In contrast to an austenitic microstructure of wrought SS, CASS alloys consist of a dual-phase microstructure of delta ferrite and austenite. While the delta ferrite is critical for the service performance of CASS alloys, it is also vulnerable to embrittlement when exposed to reactor service temperatures and fast neutron irradiations. In this study, the combined effect of thermal aging and neutron irradiation on the degradation of CASS alloys was investigated. Static casts of CF-3 and CF-8 grades with > 23% delta ferrite were selected for the study, and specimens with and without prior thermal aging were irradiated at ~320°C to about 0.08 dpa. Crack growth rate and fracture toughness J-integral resistance curve tests were performed in simulated light water reactor environments with low corrosion potential. While no elevated crack propagation rates were detected, significant reductions in fracture toughness were observed after either thermal aging or neutron irradiation. The loss of fracture toughness due to neutron irradiation seemed more evident in the samples without prior thermal aging. Transmission electron microscope (TEM) examination showed that both neutron irradiation and thermal aging affect the microstructural evolution of delta ferrite. A high density of G-phase precipitates was observed in both thermally aged and irradiated specimens. The evolution of the precipitate microstructure is more extensive in the samples subjected to both thermal aging and neutron irradiation. The similarity of precipitate microstructures resulting from thermal aging and neutron irradiation are consistent with the fracture toughness results, suggesting a common microstructural origin of the observed embrittlement among the tested specimens.

Keywords

Irradiation embrittlement, cast austenitic stainless steels, crack growth rate, fracture toughness, irradiation defects, and G-phase precipitates

1. Introduction

As a near-net-shape manufacturing process, casting is a valuable method for fabricating reactor components with complex shapes, such as cooling pipes, elbows, pump casings, valve bodies, etc. In light water reactors (LWRs), the CF grades cast austenitic stainless steels (CASS) are the most common castings used, alongside with wrought stainless steels (SS), for primary pressure boundaries and reactor core internals [1]. Similar to 300 serial of SSs, the CF grades have high contents of Cr (17-21%) and Ni (8-11%), and exhibit excellent corrosion resistances and mechanical properties. The ASME SA-351 CF-3 and CF-8 alloys are found to be highly resistant to oxidation in a variety of acids and aqueous environments [2]. The yield strength and ductility of the CF grades are also comparable to that of wrought SSs, giving rise to their excellent fracture resistances [3]. Chopra and Sather [4] showed that the crack initiation toughness of CF-3 and CF-8 CASS alloys at room temperature varies from 200 kJ/m^2 to over 1000 kJ/m^2, comparable to those of wrought SSs reported by Mills [5].

The CF grades of CASS alloys consistent a dual-phase microstructure of delta ferrite and austenite. The dual-phase microstructure is critical for the soundness, weldability, strength, and corrosion resistance of CASS alloys. Dictated by the alloy's composition, a CASS alloy solidifies from liquid phase with primary ferrite. A ferrite-to-austenite transformation follows during cooling, resulting a final mixture of retained ferrite and austenite [6]. The precise fraction of ferrite phase varies from a few percent to over ~30-40%, and is controlled by the alloy's composition and cooling rate [2][7].

The ferrite phase plays an important role in the service performance of CASS alloys. Since hardening by thermal-mechanical treatments cannot be easily implemented in castings, the strength of CASS alloys mainly rely on the presence of ferrite phase which is typically much harder than the austenite matrix. Beck et al. [8] has showed that, at both room and elevated temperatures, the tensile and yield strength of CASS increases with the content of delta ferrite up to 40%. The ferrite phase is also crucial for the soundness and weldability of steel castings. To reduce the tendency of hot cracking, a minimum ferrite content is often required for SS welds. In addition, the presence of ferrite phase can also improve the resistance to sensitization and stress corrosion cracking (SCC). In susceptible environments, CASS alloys containing ferrite tend to be more resistant to SCC than the same grade of wrought SSs [9][10].

While mostly beneficial, the presence of delta ferrite can also exert a detrimental effect under certain conditions on the fracture resistance of CASS alloys. Exposed to elevated temperatures, the delta ferrite

is vulnerable to thermal aging embrittlement [11][12][13]. The fracture toughness of CASS alloys are found to be The extent of thermal aging embrittlement increases with ferrite content and is sensitive to the ferrite morphology [4]. In addition, CASS alloys used in reactor core internals can also be damaged by fast neutron irradiations. Irradiation-induced defects can seriously affect the fracture resistance of CASS alloys, leading to additional embrittlement. While the thermal aging and irradiation embrittlement have been studied separately in the past, the combined effect of neutron irradiation and thermal aging on the fracture resistance of CASS alloys is not clear at present. Very limit data are available on the fracture resistance of CASS alloys under a combination of neutron irradiation and thermal aging [14]. In this study, the combined effect of thermal aging and neutron irradiation on CASS alloys was investigated. Neutron-irradiated CASS specimens with and without prior thermal aging were tested in simulated LWR environments for crack growth rate and fracture toughness. Transmission electron microscope (TEM) examination was also carried out to understand the damage mechanisms resulting from thermal aging and neutron irradiation.

2. Experimental

2.1 Materials and Samples

The ASME SA-315 CF-3 and CF-8 are the cast grades used extensively in the reactor cooling systems and core internals of LWRs. Two heats of CASS alloys, CF-3 and CF-8, were selected for this study. Both heats were static castings with 23-24% ferrite. Table 1 shows their compositions. Both as-cast (i.e., unaged) and thermally aged materials are included in this study. The thermal aging was conducted at 400°C for 10,000 h to emulate long-term thermal aging effects in service. This thermal aging condition has been shown to produce significant declines in Charpy impact energies in CASS alloys at both room and elevated temperatures [4].

For crack growth rate and fracture toughness J-R curve tests, sub-sized compact-tension (CT) specimens were used. The sample was about 6.5-mm thick (i.e., 1/4T-CT) and 14 mm high. The starter notch size was about 6 mm. To ensure an in-plane crack growth, side grooves approximately 5% of the sample thickness were machined on both sides of the sample. Fig. 1 shows a schematic of the 1/4T-CT sample.

2.2 Irradiation

All samples were irradiated in a helium-filled capsule at the Halden reactor in Norway. The irradiation temperature was ~320°C, and two sets of melting alloy temperature monitors were installed in the

irradiation assembly. Neutron fluence was monitored with flux wires located outside the irradiation capsule. Based on the dosimetry, the estimated fast neutron fluence (E > 1MeV) was about 5.56×10^{19} n/cm^2, corresponding to a displacement damage of 0.08 displacement per atom (dpa) for stainless steels.

2.3 Crack growth rate test

Crack growth rate (CGR) tests were performed in the Irradiated Materials Laboratory, a hot-cell facility at Argonne National Laboratory (ANL). Two servo-hydraulic testing systems were set up inside the hot cells along with water recirculating loops. The tests were conducted either in high-purity water with less than 10 ppb dissolved-oxygen (DO) or in simulated PWR water with hydrogen addition, both environments are known to reduce the sensitivity of SSs to corrosion-fatigue and SCC [15]. The conductivity of low-DO high-purity water was kept below 0.07 μS/cm during the tests. The simulated PWR water contained ~2 ppm lithium and ~1000 ppm boron, and its conductivity was about 20 μS/cm. During the tests, water was circulated at a rate of 20-30 mL/min, and the temperature and pressure of the autoclaves were kept at ~315°C and ~1800 psig, respectively.

All specimens were precracked in the test environment at ~315°C with a triangular waveform at a load ratio of 0.2 and 1 Hz frequency. The maximum stress intensity factors (K_{max}) were about 17 MPa m$^{1/2}$ for the irradiated specimens and slightly lower (~15 MPa m$^{1/2}$) for the unirradiated samples. The crack length was measured continuously with a direct current potential drop (DCPD) across the crack mouth of the specimens.

Following an initial precracking stage, environmentally enhanced cracking was induced by a series of cyclic loading steps with gradually increased rise times and load ratios. Once the environmentally enhanced cracking was stabilized, the cyclic CGR test was transitioned to a SCC test under a quasi-static load with or without periodical partial unloading (PPU). SCC CGRs were then measured at one or two stress intensity factors (Ks). At each K, a near constant-K loading condition was maintained during the test period by gradually reducing the load as the crack propagated.

2.4 Fracture toughness J-R curve test

After the SCC CGR test, a fracture toughness J-R curve test was carried out in the same test environment and temperature. Using the SCC crack as a starter crack, the sample was loaded in tension at a constant displacement rate of 4.3×10^{-7} m/s while the load and sample extension were recorded continuously. During the J-R curve test, the loading was interrupted periodically and the sample was held at a constant extension for a crack-length measurement with DCPD. After the test, a J integral value was calculated at each crack extension, and the data were fitted to a power-law expression to obtain a J-resistance curve.

After the J-R tests, the specimens were fractured in air at room temperature. The fracture surfaces of unirradiated control samples and replicas of irradiated samples were examined using a scanning electron microscope (SEM). The CGR and J-R curve results were corrected by scaling the final crack length measured by DCPD to the crack size measured with SEM.

2.5 Microstructural examination

The CASS materials were also examined with TEM in this study. The TEM disks were electrochemically polished with a twin-jet polisher at -35°C in an electrolyte of 5% perchloric acid and methanol. The obtained thin foils were examined with a Hitachi-H9000 TEM at the Intermediate Voltage Electron Microscopy (IVEM) facility at ANL.

3. Results and Discussion

3.1 Cyclic crack growth rates

The corrosion fatigue and SCC responses of the CASS materials were evaluated with crack propagation rates under cyclic load and near constant-K conditions, respectively. The sample was precracked from the machined notch in the test environments. The crack was then advanced with cyclic load in a serial of test periods with gradually increased rise time and load ratio while the K_{max} was kept approximately a constant. A time-based cyclic growth rate (CGR_{env}) was measured for each test period. Fig. 2 shows a typical crack extension history plot during a cyclic CGR test.

For each loading condition, a fatigue CGR in air (CGR_{air}) was estimated with the same load parameters (i.e., load ratio and rise time) based on a correlation developed by James and Jones [16]. Fig. 3 shows a typical dataset of cyclic CGR_{env} as a function of calculated CGR_{air}. Moderate CGRs higher than the estimated fatigue growth rates in air were observed for all CASS specimens, particularly below 10^{-9} m/s.

In general, the corrosion fatigue responses of the CASS samples were sluggish in this study. Crack growth was frequently stalled, and repeated attempts were needed to re-active and stabilize the crack growth. Significant data scatters more than a factor of five can be seen among the cyclic CGR data. Note that, due to the complex nature of test control and crack growth monitoring, a high uncertainty in CGR measurements is not unexpected in this type of tests. With identical material and test conditions, the differences in CGR measurements are quite often exceed a factor of tow under normal experimental conditions. The higher than normal uncertainties in the current tests is partially due to the limited test time and slow CGRs in the low-corrosion-potential environments.

To evaluate the extent of environmentally enhanced cracking, the cyclic CGR data are plotted against fatigue CGRs in air and fitted to a superposition model for each specimen. By assuming that the environmental contribution to cyclic CGRs is related to fatigue crack growth rate in air, Shack and Kassner [17] determined the corrosion fatigue curves for unirradiated wrought and CASS SSs in high-purity water containing low-DO (0.2 PPM). Using this corrosion fatigue curve as a reference, the best fit curves for all data sets are compared in Fig. 4. All fitting curves, regardless their thermal aging conditions or irradiation histories, are bounded by the reference line, suggesting adequate corrosion-fatigue responses of CASS alloys in the low-corrosion-potential environments. Also, the neutron irradiation at ~320°C to 0.08 dpa does not increase the cracking susceptibility of the CASS alloys. Given the large data scatter among these tests, these differences are not statistically significant. It is clear that these CASS alloys exhibit excellent corrosion-fatigue resistances in the low-corrosion-potential environments.

3.2 SCC crack growth rates

The good resistances to environmentally enhanced cracking are also observed in the SCC tests for the CASS alloys. All SCC CGRs obtained in this study (with or without irradiation) are plotted in Fig. 5 along with the NUREG-0313 disposition curve, a reference curve obtained with sensitized SSs in BWR normal water chemistry [18]. The open symbols are unaged CASS, and the closed symbols are their aged counterparts. All data points are well below the NUREG-0313 line, and moderate CGRs in the range of 10^{-11} m/s are only obtained under loading conditions with PPU. Without PPU, the measured CGRs are much lower, and sometime below the detectable limit of the DCPD measurement. An accurate determination of such a low growth rate would require a much longer test time than possible in the current study.

The unaged and aged data sets, regardless of their grades and test conditions, are fitted to a power-law expression with a power exponent of 2.16 – the same value used in developing NUREG-0313 curve. As shown in Fig. 5, the fitting curves of the unaged specimens are just slightly higher than the aged ones. This difference between the unaged and aged results is also insignificant given the large data scatter and inherent uncertainty in short CGR tests like these. Thus, thermal aging seems not to affect the cracking susceptibility in the low-DO high-purity and PWR water. This lack of sensitivity to thermal aging history is consistent with that observed in the cyclic CGR tests.

Corrosion potential has a profound impact on crack growth behavior [15]. In BWR water, the SCC CGRs measured in low-corrosion potential environment, i.e., hydrogen water chemistry (HWC), is more than one order of magnitude lower than that measured in normal water chemistry (NWC) [19]. This strong effect of corrosion potential has been observed in both unirradiated and irradiated wrought SSs. In CASS alloys, the presence of ferrite is also a significant factor for lowering the cracking susceptibility. It has been shown in unirradiated CASS materials that a dual-phase microstructure is more resistant to SCC than single-phase wrought SSs in high-DO water [9][10]. The superior SCC performance of the duplex microstructure may arise from the deformation behavior of the ferrite phase. It has been showed that the hardness of ferrite phase is much higher than that of austenite phase [20]. Consequently, the plastic deformation is developed to a less extent in the ferrite than in the austenite. By delaying the development of heavy plastic deformation in ferrite phase, a slip-dissolution mechanism could be hindered to some extent in a duplex microstructure. It is not clear, however, if this beneficial effect of ferrite could be diminished by thermal aging or irradiation embrittlement. A deteriorated fracture resistance of ferrite grains would accelerate the development of plastic strain in the surrounding austenite. Elevated SCC CGRs were indeed observed in a thermally aged CF-8M irradiated to ~2.4 dpa in normal water chemistry [14]. This observation suggested that the beneficial effect of a duplex microstructure could be greatly reduced by neutron exposure to a sufficiently high fluence level, at least in high-corrosion-potential environments. Nonetheless, in the current study, the neutron irradiation up to 0.08 dpa does not appear to affect the cracking susceptibility of CASS alloys in the low-corrosion-potential environments.

3.3 Fracture toughness

Fig. 6 shows a typical J-R curve test result obtained in this study. A J-integral was calculated at each crack extension measured by DCPD according to ASTM Specification E 1820. A J-R curve is constructed by fitting the calculated J values to a power law relationship with crack extension, $J=C*\Delta a^n$. Note that, because of the low strength and high fracture toughness of the CASS materials, the required crack tip constraint and upper limit of J integral were often invalid with the 1/4T-CT specimens used in the current study. Thus, the obtained J values are not always validated for JIC per ASTM E1820. Also, a blunting line of four times the flow stress (i.e., $J/4\sigma_f$) recommended by Mills [5] has been used in J-R curve analysis in the current study.

Table 2 summaries all J-R curves obtained in this study. The fitting parameters C and n are reported along with the J_Q values at the intersections of the power law curves and the 0.2-mm offset blunting lines. Note that for the specimen of unaged and unirradiated CF-8, a J value at the end of the test is reported because a full J-R curve is unavailable. The total crack extension was insufficient for this test due to significant crack tip blunting.

Fig. 7 shows all J-R curves obtained in this study. An estimated J-R response is used for the unaged and unirradiated CF-8 specimen. Both the CF-3 and CF-8 alloys exhibit excellent fracture resistances in the unaged and unirradiated condition. After the thermal aging, the J-R curves are reduced considerably. This is consistent with what observed in previous studies, in which significant reductions in Charpy impact energies were observed after thermal aging at 400°C for 10,000 h [4][21].

The effect of neutron irradiation is evident, even at such a low dose (i.e., 0.08 dpa). For the unaged specimens, the J-R curves are lowered considerably after irradiation. The irradiated J-R curve for the unaged CF-3 is between the two unirradiated curves (as shown in Fig. 7a), and the irradiated J-R curve for the unaged CF-8 is below its aging-only counterpart (as shown in Fig. 7b). The dotted line in Fig. 7b is the initial part of the J-R curve test result on the unaged and unirradiated specimen. Since very little crack extension was obtained in this test, no data points outside the exclusion zone were available for the power-law curve fitting. For the aged specimens, the J-R curves are also lowered after irradiation, but the magnitudes of the reductions appear to be less than that of unaged specimens. For both CF-3 and CF-8, the extent of irradiation embrittlement is more evident in the unaged specimens. It appears that the irradiation-induced deterioration was developed more rapidly in the unaged than the aged

CASS specimens. Consequently, the differences in fracture toughness between the unaged and aged specimens were reduced after irradiation. This change suggests a dominant role of neutron irradiation (compared to thermal aging) in promoting embrittlement in CASS alloys.

3.4 Microstructural examination

Both the CF-3 and CF-8 showed a typical casting microstructure with coarse austenitic grains and vermicular ferritic regions. In the unaged and unirradiated specimens, a very low dislocation density was observed in both ferrite and austenite phases. After thermal aging at 400°C for 10,000 h, the austenitic phase remained unchanged. In ferritic phase, however, a high density of nm-scale particles was observed as shown in Fig. 8. Using their diffraction pattern, these precipitates were identified as G-phase precipitates, a nickel silicide (M6Ni16Si7) with a fcc crystal structure. Note that the dark-field images shown in Fig. 8 were formed with G-phase reflection spots.

The neutron irradiation at ~320°C to 0.08 dpa did not affect the austenitic phase significantly. Very few "black-dot" defects were visible in the austenite after irradiation as shown in Fig. 9. In the areas with pre-exiting dislocations, the dislocation lines were decorated with large loops as shown in Fig. 10. In the areas where the pre-existing dislocations are absent, irradiation-induced defects may be too small to be visible under TEM. In general, the neutron irradiation conducted in this study has little effect on the austenite at the current dose level (~0.08 dpa).

In contrast to the relatively weak effect observed in the austenite, the neutron irradiation had a strong impact on the ferrite. Without thermal aging, a high-density of nm-scale features appeared in the ferrite after irradiation. A detailed analysis with bright-field and dark-field images indicates that these particles are mostly G-phase precipitates, rather than irradiation-induced defect-clusters or dislocation loops (see Fig. 11). Fig. 12 shows the dark-field images with G-phase reflection. The similarity between the precipitate microstructures in Fig. 8 and Fig. 12 is evident. Since the precipitation process can occur under either thermal aging or neutron irradiation, a combination of thermal aging and neutron irradiation may yield a more extensive microstructural evolution. As shown in Fig. 13, the density of G-phase precipitates appears even higher in the irradiated specimens with prior aging.

The TEM result is used to understand the embrittlement observed in the J-R curve tests. The micro-mechanisms responsible for the thermal aging embrittlement of CASS alloys are well understood

[11][12][13]. A miscibility gap in the Fe-Cr system gives rise to a spinodal decomposition of two ferrite phases, a Fe-rich α phase and a Cr-rich α' phase. The redistribution of Cr within ferrite phase is accompanied by the rearrangement of other alloying elements, which can lead to additional nucleation and growth of precipitates within the ferrite phase or at the ferrite-austenite boundaries. Thus, carbides and Ni-rich G-phase can also be the main contributors to the thermal aging embrittlement. The microstructurale observations on the unirradiated CASS specimens seem to confirm this embrittlement mechanism (Fig. 8).

The kinetics of this embrittlement mechanism may be affected by neutron irradiation. The super saturation of point defects induced by irradiation could play a key role in the microstructural evolution, leading to precipitation and phase separation behaviors different from that under equilibrium conditions [22]. A comparison of the precipitate microstructures between the aged-only (Fig. 8) and irradiated-only specimens (Fig. 12) confirms the important role of irradiation. While the thermally-induced and irradiation-induced precipitate microstructures are similar, both the precipitate size and density are higher in the irradiated specimens (Fig. 12) than in the aged specimens (Fig. 8). Yet, the highest density of G-phase precipitates are is seen in the irradiated specimens with prior aging (Fig. 13). It is clear that the thermal aging or neutron irradiation alone can produce similar precipitate microstructures, and the combination of thermal aging and neutron irradiation may lead to more extensive precipitation in the ferrite. Since the G-phase precipitation is closely related to the α/α' phase separation [23][24], it is reasonable to assume that the phase separation has occurred in the aged, irradiated, and aged+irradiated specimens. In a parallel study performed with atom probe tomography, the α/α' phase separation was indeed observed along with the G-phase precipitation in CASS alloys [25].

These microstructural observations imply that both thermal aging and neutron irradiation can embrittle the CASS alloys, and the two degradation processes are interrelated. This is consistent with the J-R curve test results. Both the thermal aging at 400°C for 10,000 h and neutron irradiation at ~320°C to 0.08 dpa alone can decrease the fracture resistance of CASS alloys considerably. The combination of aging and irradiation can lead to some additional loss of fracture toughness. It appears that neutron irradiation conducted in this study enables or facilitates the precipitation or phase separation that would otherwise occur too slowly at the irradiation temperature. Since the precipitation and phase separation processes responsible for the thermal aging embrittlement and irradiation embrittlement are the same, the two degradation mechanisms are not independent but related in CASS alloys.

4. Conclusion

Crack growth rate and fracture toughness J-R curve tests were performed at ~315°C in low-corrosion-potential environments on the unaged and aged CF-3 and CF-8 specimens with 23-24% ferrite. The samples were irradiated at ~320°C to a total dose of 0.08 dpa. All CASS specimens showed good corrosion-fatigue and SCC responses in the tested environments regardless of their thermal aging history or irradiation condition.

The neutron irradiation had a significant embrittlement effect on the unaged CASS specimens, and the fracture toughness of the unaged CASS samples was reduced considerably after irradiation. A further decline in fracture toughness was also observed for the aged specimens after irradiation, suggesting additional damage resulting from the combination of thermal aging and neutron irradiation.

G-phase precipitates were observed with TEM for the aged, and irradiated CASS specimens with and without prior aging. While the precipitate microstructure was similar after only aging or irradiation, a more extensive precipitate microstructure can be seen in the aged+irradiated samples. The neutron irradiation conducted in this study seems to facilitate the development of G-phase precipitates. The two degradation mechanisms, i.e. thermal aging and neutron irradiation, appear to be related and can interact at a microstructural level.

Acknowledgements

The authors would like to thank Drs. O. K. Chopra and W. J. Shack for their contribution to this project. We also would like to thank Ms. T. M. Karlsen, OECD Halden Reactor Project, Halden, for assistance with irradiations and specimen transfer. Drs. J. Pakarinen and Y. Huang of University of Wisconsin-Madison are acknowledged for their contributions to the experimental effort. This work is sponsored by the U.S. Nuclear Regulatory Commission, under Job Code N6519, and by the U.S. Department of Energy, under contract # DE-AC02-06CH11357.

References:

[1] U.S. NRC (2006), “Expert Panel Report on Proactive Materials Degradation Assessment,” NUREG/CR-6923.

[2] M. Blair, T. L. Stevens, “Corrosion-Resistant High Alloy Steels,” in Steel Castings Handbook, 6th Edition, Steel Founders’ Society of America and ASM International, 1995.

[3] ASTM International, “Standard Specification for Castings, Austenitic, for Pressure-Containing Parts,” A351/A351M-10, Annual Book of ASTM standards, 2012.

[4] O. K. Chopra, and A. Sather (1990), “Initial Assessment of the Mechanisms and Significance of Low-Temperature Embrittlement of Cast Stainless Steels in LWR Systems,” NUREG/CR-5385, ANL-89/17.
[5] W. J. Mills, International Materials Reviews, 4, No.2 (1997): 45.
[6] J. W. Elmer, S. M. Allen, and T. W. Eagar, Metallurgical Transactions A, 20A, (1989) 2117.
[7] L. S. Aubrey, P. F. Wieser, W. J. Pollard, and E. A. Schoefer (1982) “Ferrite Measurement and Control in Cast Duplex Stainless Steel,” in Stainless Steel Castings, ASTM STP 756, pp. 126-164.
[8] F. H. Beck, E. A. Schoefer, J. W. Flowers, and M. G. Fontana (1965), "New Cast High-Strength Alloy Grades by Structure Control," in Advances in the Technology of Stainless Steels and Related Alloys, ASTM STP 369.
[9] F. H. Beck, J. Juppenlatz, and P. F. Wieser (1976), “Effects of Ferrite and Sensitization on Intergranular and Stress Corrosion Behavior of Cast Stainless Steels,” in Stress Corrosion - New Approaches, H. L. Craig, Jr., ed., ASTM STP 610.
[10] N. R. Hughes, W. L. Clarke, and D. E. Delwiche (1982), “Intergranular Stress-Corrosion Cracking Resistance of Austenitic Stainless Steel Castings,” in Stainless Steel Castings, V. G. Behal and A. S. Melilli, eds., ASTM STP 756.
[11] R. M. Fisher, E. J. Dulis, and K. G. Carroll (1953), Transactions of AIME 197, No. 5, pp. 690–695.
[12] P. J. Grobner (1973), Metallurgical and Materials Transactions B, 4, No. 1, pp. 251-260.
[13] T. J. Nichol, A. Datta, and G. Aggen (1980), Metallurgical and Materials Transactions A, 11, No. 4, pp. 573-585.
[14] O. K. Chopra, and W. J. Shack (2008), “Crack Growth Rates and Fracture Toughness of Irradiated Austenitic Stainless Steels in BWR Environments,” NUREG/CR-6960, ANL-06/58.
[15] P. L. Andresen, F. P. Ford, S. M. Murphy, and J. M. Perks, “State of Knowledge of Radiation Effects on Environmental Cracking in Light Water Reactor Core Materials,” Proc. 4th Intl. Symp. on Environmental Degradation of Materials in Nuclear Power Systems -- Water Reactors, NACE, Houston, TX, pp. 1.83-1.121, 1990.
[16] L. A. James, and D. P. Jones, “Fatigue Crack Growth Correlation for Austenitic Stainless Steels in Air,” Proc. Conf. on Predictive Capabilities in Environmentally-Assisted Cracking, PVP Vol. 99, R. Rungta, ed., American Society of Mechanical Engineers, New York, pp. 363-414, 1985.
[17] W. J. Shack, and T. F. Kassner, “Review of Environmental Effects on Fatigue Crack Growth of Austenitic Stainless Steels,” NUREG/CR-6176, ANL-94/1, 1994.
[18] W. S. Hazelton, and W. H. Koo, “Technical Report on Material Selection and Processing Guidelines for BWR Coolant Pressure Boundary Piping,” NUREG-0313, Rev. 2, 1988.
[19] Y. Chen, O. K. Chopra, E. E. Gruber, W. J. Shack, “Irradiation-assisted stress corrosion cracking of austenitic stainless steels in BWR environments,” NUREG/CR-7018, 2010.
[20] Z. Wang, F. Xue, J. Jiang, W. Ti, and W. Yu, Engineering Failure Analysis, 18 (2011): 403.
[21] O. K. Chopra (1994), “Estimation of Fracture Toughness of Cast Stainless Steels During Thermal Aging in LWR Systems,” NUREG/CR-4513 Rev. 1, ANL-93/22.
[22] F. A. Garner, J. M. McCathy, K. C., Russell, and J. J. Hoyt, Journal Nuclear Materials, 205 (1993): 411.
[23] F. Danoix, P. Auger, D. Blavette, Surface Science 266, 1-3 (1992): 364-369.
[24] F. Danoix, P. Auger, S. Chambreland, D. Blavette, Microscopy Microanalysis Microstructures, 5 (1994) 121-132.
[25] Z. Li, Y. Chen, A. S. Rao, and Y. Yang, J. Nucl. Mater., 466 (2015): 201.

List of tables:

Table 1 Compositions of the CASS alloys
Table 2 Fracture toughness test result

List of figures:

Fig. 1 Schematic of 1/4T-CT specimen and their nominal dimensions in mm.
Fig. 2 An example of crack extension history plot of cyclic CGR tests
Fig. 3 Cyclic CGR test result of Specimen A-2, an unaged CF-3 CASS irradiated to 0.08 dpa.
Fig. 4 Best-fit curves of cyclic CGRs: (a) unaged and aged CF-3, and (b) unaged and aged CF-8.
Fig. 5 SCC CGRs of the unaged and aged CASS materials in low-DO high-purity and PWR water environments.
Fig. 6 A typical J-R curve obtained from 1/4T-CT specimen.
Fig. 7 Power-law curve fitting results of J-R data of (a) CF-3, and (b) CF-8 alloys tested at ~315°C.
Fig. 8 Dark-field images of the ferritic phase for the unirradiated CF-3 (a) and CF-8 (b) after thermal aging. The insert shows the diffraction pattern close to 001 zone. The labels G and F indicate the diffraction spots from the G-phase and ferrite, respectively
Fig. 9 Bright-field (a) and Dark-field (b) images of the austenite phase in the unaged CF-3 irradiated to 0.08 dpa at ~320°C. The diffraction condition was g = 200 (g, 2g) and (g, 4g) for bright-field and dark-field, respectively.
Fig. 10 Bright-field images of the austenite phase in the irradiated CF-8 without (a) and with prior aging (b). The diffraction condition was g = 200 (g, 2g).
Fig. 11 TEM micrographs with different imaging conditions of an area in the irradiated CF-8 with prior aging. Label A: features visible in all of bright-field (BF), dark-field (DF) and dark-field formed with G-phase precipitate spot (DFG); Label B: features visible in both BF and DFG; Label C: features visible only in DFG, invisible or weak in BF and DF; Label D: visible in DFG and DF, invisible or very weak in BF. Label F, features visible in BF or DF, but invisible in DFG.
Fig. 12Dark-field images of the ferrite phase in the aged CF-8 irradiated to 0.08 dpa at ~320°C. The diffraction spot of G-phase precipitates was used to form the dark field image.
Fig. 13 Dark-field images of the ferrite phase in the aged CF-8 irradiated to 0.08 dpa at ~320°C. The diffraction spot of G-phase precipitates was used to form the dark field image.

Table 1 Compositions of the CASS alloys

Casting	Composition (wt. %)								
	Mn	Si	P	S	Mo	Cr	Ni	N	C
CF-3	0.63	1.13	0.015	0.005	0.34	20.18	8.59	0.028	0.023
CF-8	0.64	1.07	0.021	0.014	0.31	20.46	8.08	0.062	0.063

Table 2 Fracture toughness test result

Material	Aging condition	Dose (dpa)	C	n	J_Q [1] (kJ/m^2)
CF-3	Unaged	0	536	0.68	320
	Unaged	0.08	430	0.64	204
	Aged	0	353	0.66	170
	Aged	0.08	362	0.85	116
CF-8	Unaged [2]	0	-	-	>500
	Unaged	0.08	359	0.57	183
	Aged	0	395	0.58	220
	Aged	0.08	372	0.62	171

[1] J value at the 0.2-mm offset line

[2] A full J-R curve is unavailable due to insufficient crack extension resulting from the lack of crack tip constraint. The data point at the end of the test is reported here.

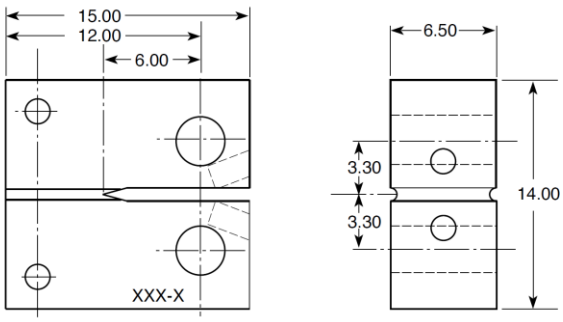

Fig. 1 Schematic of 1/4T-CT specimen and their nominal dimensions in mm.

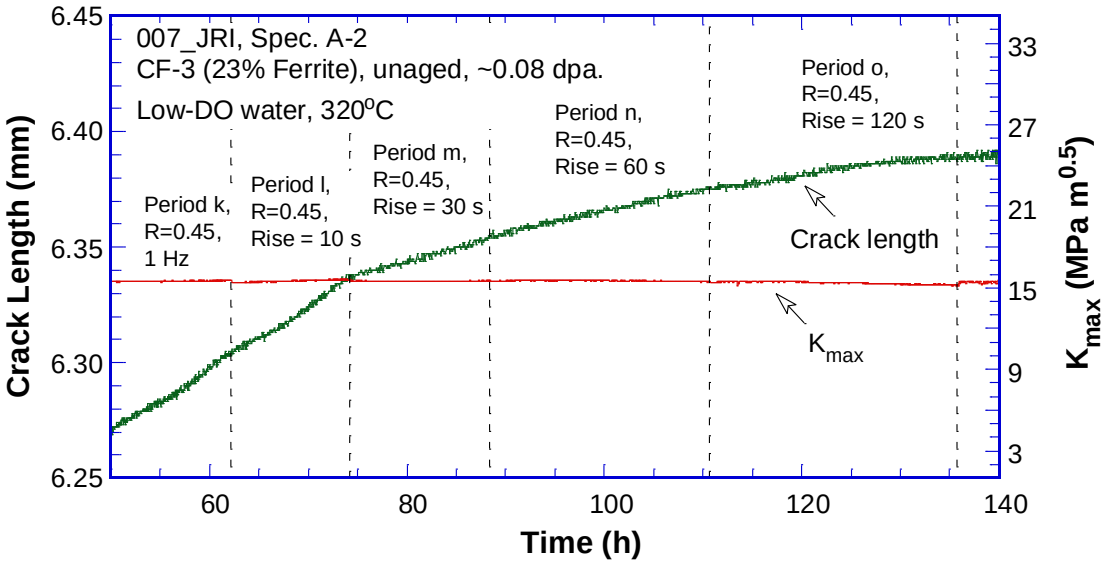

Fig. 2 An example of crack extension history plot of cyclic CGR tests

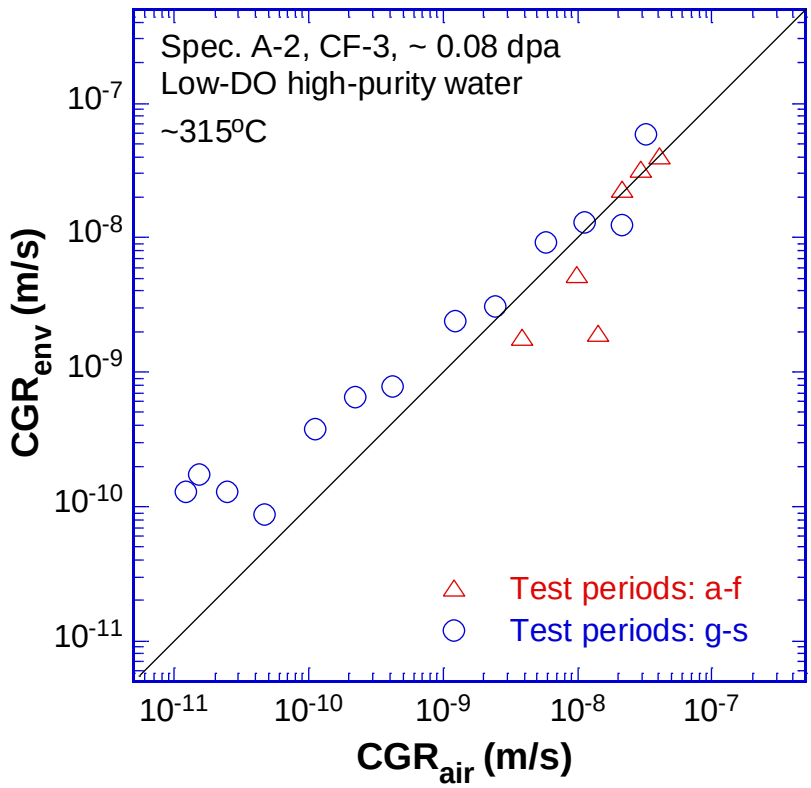

Fig. 3 Cyclic CGR test result of Specimen A-2, an unaged CF-3 CASS irradiated to 0.08 dpa.

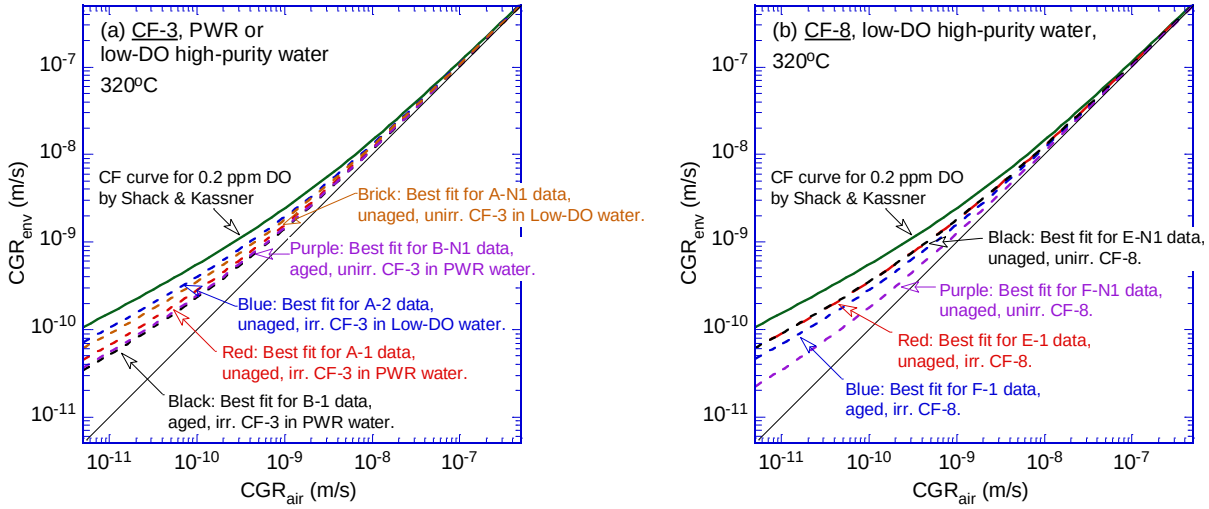

Fig. 4 Best-fit curves of cyclic CGRs: (a) unaged and aged CF-3, and (b) unaged and aged CF-8.

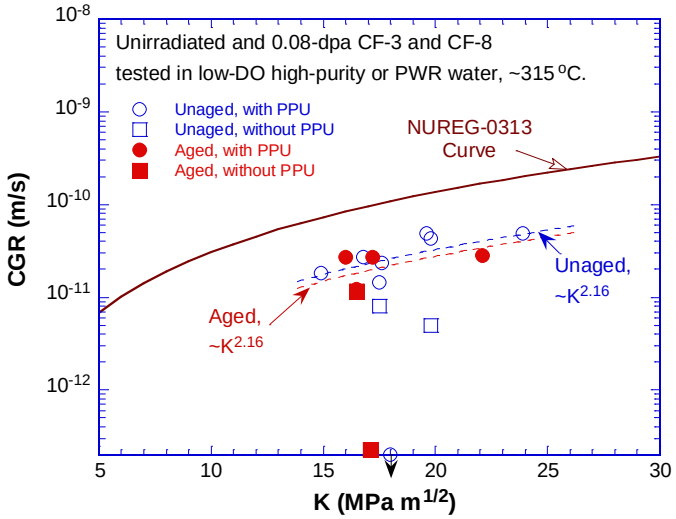

Fig. 5 SCC CGRs of the unaged and aged CASS materials in low-DO high-purity and PWR water environments.

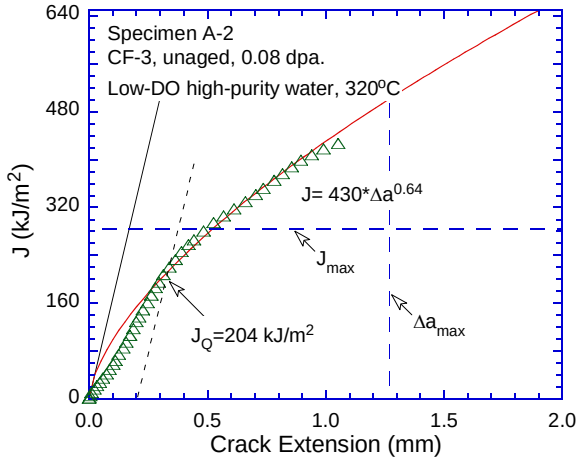

Fig. 6 A typical J-R curve obtained from 1/4T-CT specimen.

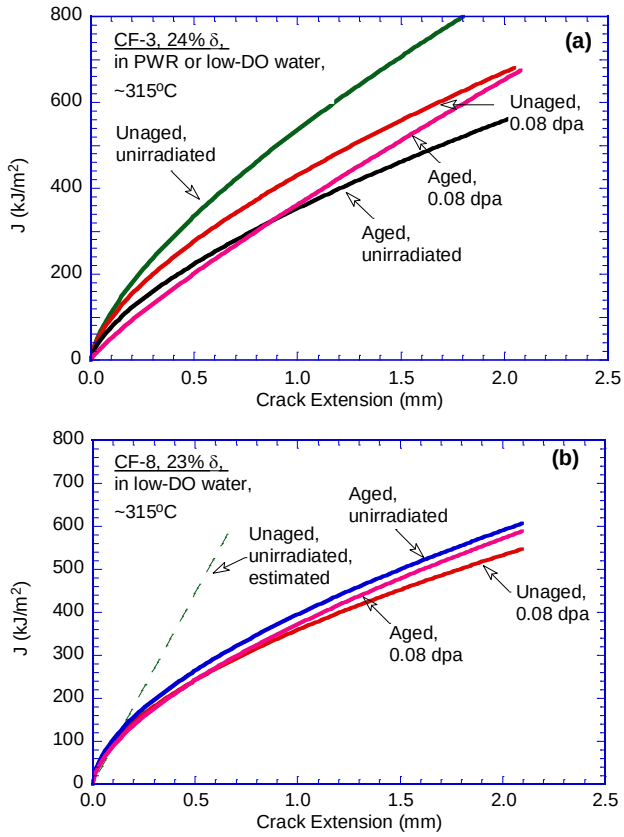

Fig. 7 Power-law curve fitting results of J-R data of (a) CF-3, and (b) CF-8 alloys tested at ~315°C.

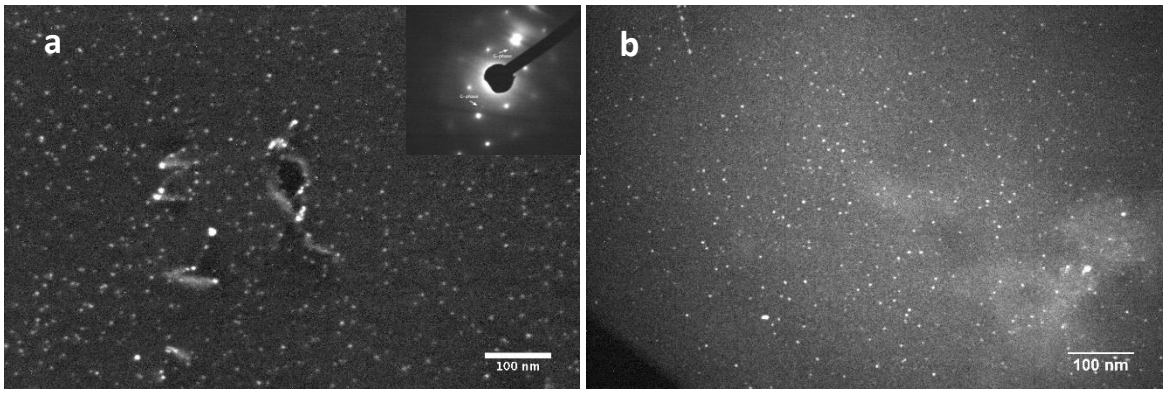

Fig. 8 Dark-field images of the ferritic phase for the unirradiated CF-3 (a) and CF-8 (b) after thermal aging. The insert shows the diffraction pattern close to 001 zone. The labels G and F indicate the diffraction spots from the G-phase and ferrite, respectively

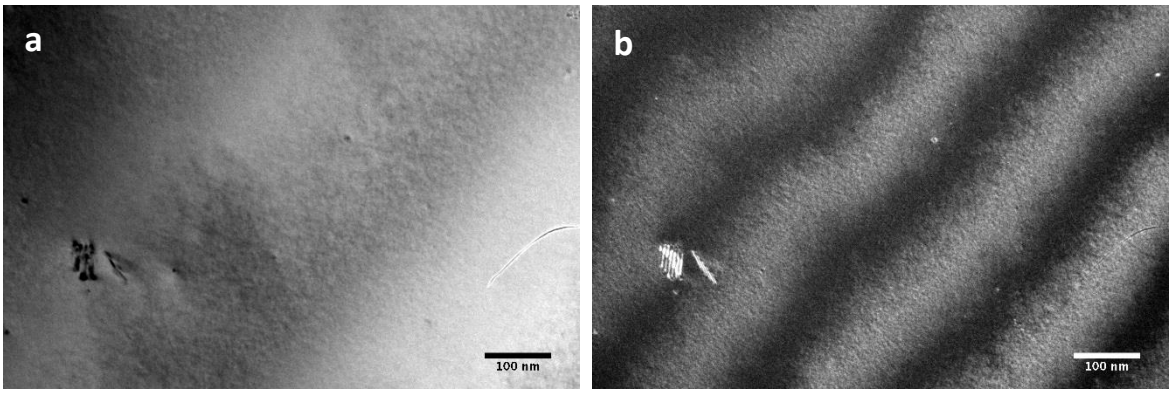

Fig. 9 Bright-field (a) and Dark-field (b) images of the austenite phase in the unaged CF-3 irradiated to 0.08 dpa at ~320°C. The diffraction condition was g = 200 (g, 2g) and (g, 4g) for bright-field and dark-field, respectively.

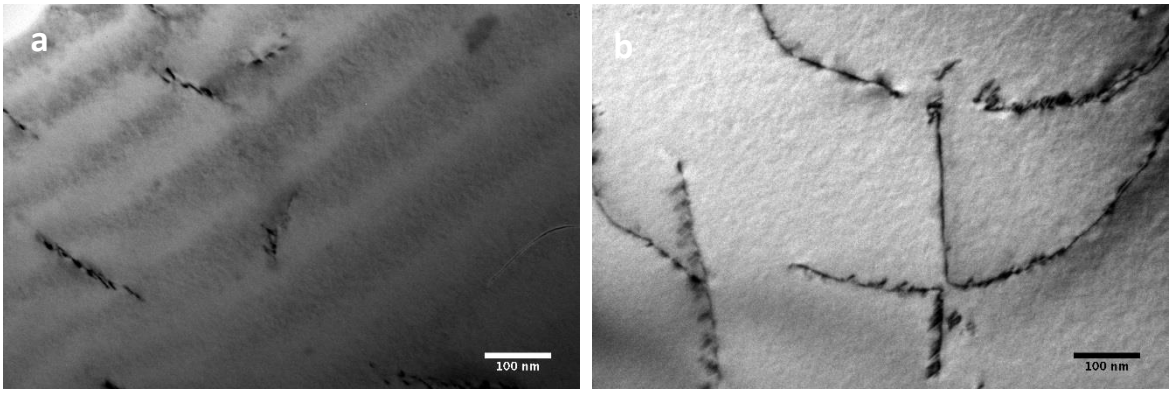

Fig. 10 Bright-field images of the austenite phase in the irradiated CF-8 without (a) and with prior aging (b). The diffraction condition was g = 200 (g, 2g).

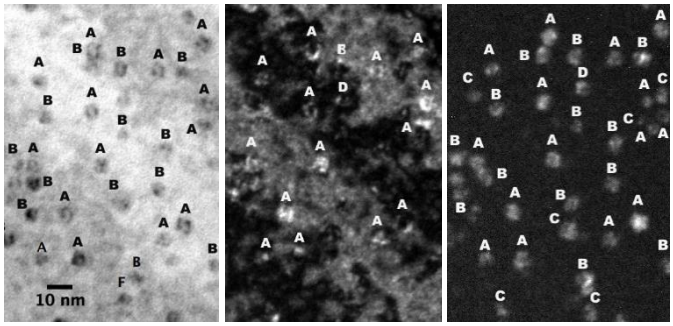

Fig. 11 TEM micrographs with different imaging conditions of an area in the irradiated CF-8 with prior aging. Label A: features visible in all of bright-field (BF), dark-field (DF) and dark-field formed with G-phase precipitate spot (DFG); Label B: features visible in both BF and DFG; Label C: features visible only in DFG, invisible or weak in BF and DF; Label D: visible in DFG and DF, invisible or very weak in BF. Label F, features visible in BF or DF, but invisible in DFG.

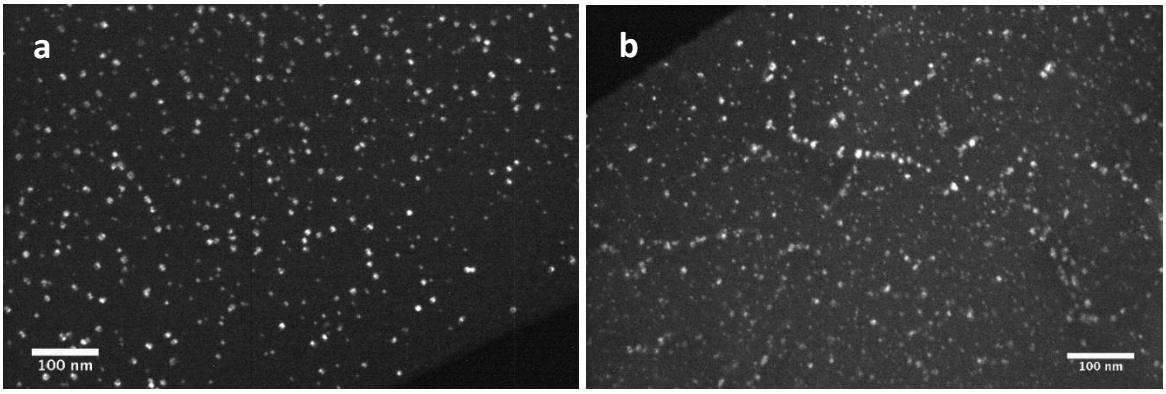

Fig. 12Dark-field images of the ferrite phase in the aged CF-8 irradiated to 0.08 dpa at ~320°C. The diffraction spot of G-phase precipitates was used to form the dark field image.

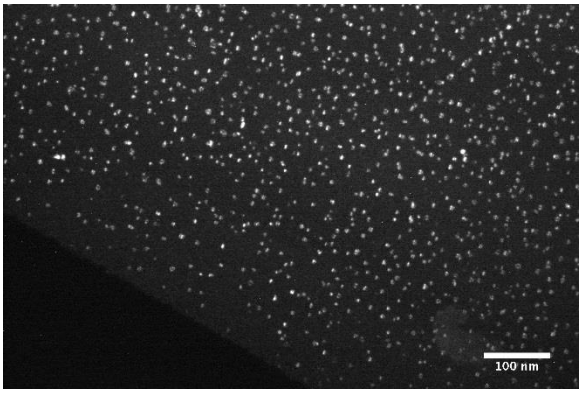

Fig. 13 Dark-field images of the ferrite phase in the aged CF-8 irradiated to 0.08 dpa at ~320°C. The diffraction spot of G-phase precipitates was used to form the dark field image.